AGU PUBLICATIONS

JGR

Journal of Geophysical Research: Atmospheres

RESEARCH ARTICLE
10.1002/2015JD024108

Key Points:
- Sensitivity of the SFI model to different reanalysis data is examined
- High-altitude (Tibetan Plateau) permafrost shows a faster thaw than high-altitude permafrost
- Permafrost in China shows the fastest thaw, followed by the United States, Russia, and Canada

Correspondence to:
D. Guo,
guodl@mail.iap.ac.cn

Citation:
Guo, D., and H. Wang (2016), CMIP5 permafrost degradation projection: A comparison among different regions, *J. Geophys. Res. Atmos.*, *121*, 4499–4517, doi:10.1002/2015JD024108.

Received 20 AUG 2015
Accepted 22 FEB 2016
Accepted article online 27 FEB 2016
Published online 7 MAY 2016

CMIP5 permafrost degradation projection: A comparison among different regions

Donglin Guo[1,3,4] and Huijun Wang[2,1]

[1]Nansen-Zhu International Research Center, Institute of Atmospheric Physics, Chinese Academy of Sciences, Beijing, China, [2]Key Laboratory of Meteorological Disaster, Ministry of Education (KLME)/Joint International Research Laboratory of Climate and Environment Change (ILCEC)/Collaborative Innovation Center on Forecast and Evaluation of Meteorological Disasters (CIC-FEMD), Nanjing University of Information Science & Technology, Nanjing, China, [3]Collaborative Innovation Center on Forecast and Evaluation of Meteorological Disasters (CIC-FEMD), Nanjing University of Information Science & Technology, Nanjing, China, [4]Climate Change Research Center, Chinese Academy of Sciences, Beijing, China

Abstract The considerable impact of permafrost degradation on hydrology and water resources, ecosystems, human engineering facilities, and climate change requires us to carry out more in-depth studies, at finer spatial scales, to investigate the issue. In this study, regional differences of the future permafrost changes are explored with respect to the regions (high altitude and high latitude, and in four countries) based on the surface frost index (SFI) model and multimodel and multiscenario data from the fifth phase of the Coupled Model Intercomparison Project (CMIP5). Results show the following: (1) Compared with seven other sets of driving data, Climatic Research Unit air temperature combined with Climate Forecast System Reanalysis snow data (CRU_CFSR) yield a permafrost extent with the least absolute area bias and was thus used in the simulation. The SFI model, driven by CRU_CFSR data climatology plus multimodel mean anomalies, produces a present-day (1986–2005) permafrost area of $15.45 \times 10^6\ \mathrm{km^2\ decade^{-1}}$, which compares reasonably with observations of $15.24 \times 10^6\ \mathrm{km^2\ decade^{-1}}$. (2) The high-altitude (Tibetan Plateau) permafrost area shows a larger decreasing percentage trend than the high-latitude permafrost area. This indicates that, in terms of speed, high-altitude permafrost thaw is faster than high-latitude permafrost, mainly due to the larger percentage sensitivity to rising air temperature of the high-altitude permafrost compared to the high-latitude permafrost, which is likely related to their thermal conditions. (3) Permafrost in China shows the fastest thaw, which is reflected by the percentage trend in permafrost area, followed by the United States, Russia, and Canada. These discrepancies are mainly linked to different percentage sensitivities of permafrost areas in these four countries to air temperature change. (4) In terms of the ensemble mean, permafrost areas in all regions are projected to decrease by the period 2080–2099. Under representative concentration pathway (RCP)4.5, permafrost retreats toward the Arctic, and the thaw in every region mainly occurs at the southern edge of the permafrost area. Under RCP8.5, almost no permafrost is expected to remain in China, the United States, and the Tibetan Plateau. Permafrost in Russia will remain mainly in the western part of the east Siberian Mountains, and permafrost in Canada will retreat to the north of 65°N. Possible uncertainties in this study are primarily attributed to the climate model's coarse horizontal resolution. The results of the present study will be useful for understanding future permafrost degradation from the regional perspective.

1. Introduction

Frozen ground includes permafrost and seasonally frozen ground [*Lachenbruch and Marshall*, 1986]. Permafrost is defined as ground where soil temperature remains at or below 0°C continuously for at least 2 years and is widely distributed in high-latitude and high-altitude regions [*Muller*, 1947]. It is estimated that the permafrost area in the Northern Hemisphere is approximately $22.79 \times 10^6\ \mathrm{km^2}$, occupying approximately one fourth of the land area of the Northern Hemisphere [*Zhang et al.*, 1999].

A previous study indicated that approximately $11.37–36.55 \times 10^3\ \mathrm{km^3}$ of ground ice may be stored in permafrost in the Northern Hemisphere, which corresponds to an equivalent rise in sea level of 3–10 cm [*Zhang et al.*, 1999]. If these ground ice stores start to melt, there will be a substantial effect on the hydrology and water resources of the permafrost region. Additionally, permafrost is a large carbon pool; it is estimated that permafrost soils in boreal and Arctic ecosystems store almost twice as much carbon as currently present in the atmosphere [*Zimov et al.*, 2006; *Schuur et al.*, 2009]. Thus, permafrost thaw and the associated carbon release may intensify climate warming [*Schuur et al*., 2009]. In addition to these aspects, the seasonally freezing and thawing processes of the permafrost active layer can result in spatiotemporal variations of soil wetness and surface heat balance. Consequently, such variations strongly affect soil biogeochemical cycles, local hydrological processes, surface energy fluxes, and regional atmospheric circulation [*Yang et al*., 2010; *Guo et al*., 2011a, 2011b; *Li et al*., 2012]. Furthermore, from the human perspective, the economic importance of permafrost regions has increased substantially in recent decades, mainly due to the abundant natural resources present in these regions. This has resulted in a rapid expansion of the human population and associated infrastructure in the north circumpolar region [*Nelson et al*., 2002]. Severe permafrost thaw, induced by climate warming, will affect the stability of human engineering facilities in these areas [*Guo and Wang*, 2013, 2014; *Guo and Sun*, 2015].

Against the background that the global climate has become warmer during recent decades, and will probably undergo further warming in the future, the permafrost region in the Northern Hemisphere will likely incur a severe thaw. *Lawrence and Slater* [2005] projected a decrease of the permafrost area by 62% and 90% by 2100 under the B1 and A2 scenarios [*Nakicenovic et al*., 2000], respectively, determined using version 3 of the fully coupled Community Climate System Model (CCSM3). With the modified Community Land Model version 3.5 (CLM3.5), driven by the output of CCSM3, *Lawrence et al*. [2008] again projected a decrease of the permafrost area, by 83%, by 1980–2099, under the A1B scenario [*Nakicenovic et al*., 2000]. More recently, *Koven et al*. [2013] analyzed permafrost thermal dynamics in response to climate change based on direct soil temperature outputs from multiple CMIP5 (Coupled Model Intercomparison Project, phase 5) models, and their results still showed a severe loss of permafrost, albeit with a wide range of predications presented. Future permafrost dynamics have also been diagnosed using a diagnostic permafrost model driven by climate model anomalies from the CMIP5 models [*Slater and Lawrence*, 2013]. The results showed a reduction of the permafrost area by $37 \pm 11\%$ (representative concentration pathway (RCP)2.6), $51 \pm 13\%$ (RCP4.5), $58 \pm 13\%$ (RCP6.0), and $81 \pm 12\%$ (RCP8.5) by 2080–2099, relative to the permafrost area during the period 1986–2005 [*IPCC*, 2013]. In short, large-scale studies like those mentioned above project future permafrost changes across the entire Northern Hemisphere.

Nevertheless, more in-depth studies at regional scales are still required that consider the major implications of permafrost thaw from scientific aspects such as the impacts on ecosystems and climate change, as well as practical aspects such as the constructions and maintenance of the human infrastructures. A regional permafrost projection was carried out on the Tibetan Plateau by *Guo et al*. [2012], based on version 4 of the CLM driven off-line by the high-resolution output from the dynamical downscaling method. Additionally, permafrost can be divided into high-latitude and high-altitude (Tibetan Plateau) permafrost according to the geographic characteristics that induce the formation of permafrost [*Cheng and Wang*, 1982]; high-latitude permafrost is mostly regulated by latitudinal zonality, while high-altitude permafrost is mostly regulated by vertical zonality. These differences may mean that they possess different sensitivities to externally climatic forcing, which is an interesting issue yet to be examined. Additionally, the degradation of permafrost is greatly concerned by the countries that possess a considerable permafrost area because of its impacts on local hydrology and water resources, ecosystems, and human engineering facilities. The projection and comparison of permafrost changes in these countries could be quite helpful for them in evaluating their own levels of permafrost degradation, thus enabling them to develop appropriate policies ahead of any anticipated changes, for example, policies related to the utilization of water resources and the construction of the human infrastructure.

The objectives of the present study are to (1) examine the sensitivity of the surface frost index (SFI) model to different reanalysis data and evaluate the ability of the model driven by the selected reanalysis data, plus anomalies of climate models, to simulate permafrost; (2) explore the differences of future high-latitude and high-altitude permafrost degradation in terms of percentage trend; and (3) explore the differences of future permafrost degradation in four countries (Russia, Canada, the United States, and China), again in terms of percentage trend. In section 2, a brief description of the model, data, and methods is provided. In section 3, we present and analyze the results. Comparisons with previous results and discussions on potential sources of possible uncertainty are given in section 4, followed by a summary of the study's key findings in section 5.

2. Model, Data, and Methods

2.1. Model

In this study, the surface frozen index (SFI) model is used, which is defined by *Nelson and Outcalt* [1987] as

$$\mathrm{SFI} = \frac{\sqrt{\mathrm{DDF}}}{\sqrt{\mathrm{DDF}^*} + \sqrt{\mathrm{DDT}}}, \tag{1}$$

where DDF* is the sum of freezing degree days modified for snow insulation and DDT is the sum of thawing degree days computed from the sinusoidal climate. The model is a dimensionless ratio which can be calculated by some specific equations [*Nelson and Outcalt*, 1987] and four yearly climate variables (mean surface air temperatures of the warmest and coldest months, mean winter snow depth, and snow density) as input data. The model does not require information about the surface state (vegetation, soils, etc.) except for snow.

As defined, this model is a function of surface air temperature and snow. Based on this function, the model stresses the importance of climate in the formation of permafrost but additionally considers the impact of snow insulation. Because the model involves an implicit assumption of climatic stationarity, the aforementioned four climate variables are usually averaged over a certain period when they are used to drive the model. In this study, a period of 20 years is used to calculate the average. Specifically, the permafrost in a certain year (e.g., 2000) was calculated using the prior 20 year average (i.e., in this case, 1981–2000) surface air temperature, snow depth, and snow density. The value of the model has a range from 0.0 to 1.0, with a value greater than 0.6 taken as the determination of continuous and discontinuous permafrost. Notably, according to the above description, results from the SFI model actually indicate the sustainability of permafrost under a certain climate stationarity condition. Moreover, permafrost change, detected by the SFI model, generally refers to change in the upper permafrost layer (i.e., near-surface permafrost) rather than deep layers of permafrost.

The requirement of readily available climate data as well as easy and rapid computation leads to the superiority of the SFI model. This allows its application to exploring distributions of permafrost existing during historical and future periods under various climate change scenarios from general circulation models [*Nelson and Outcalt*, 1987; *Anisimov and Nelson*, 1996; *Stendel and Christensen*, 2002]. In addition, recent research indicated that the SFI model, in combination with climatic change, could provide more information than raw diagnoses based on soil temperature from the climate models for the assessment of future permafrost change [*Slater and Lawrence*, 2013]. These reasons promote the use of the SFI model in this study.

2.2. Data

Four sets of monthly reanalysis data, and their combination with the University of East Anglia Climatic Research Unit (CRU) data [*Harris et al.*, 2014], were used to test the sensitivity of the SFI model to the driving data in this study. The reanalysis data included the European Centre for Medium-Range Weather Forecasts Re-Analysis Interim (ERA-Interim) [*Dee et al.*, 2011], the National Aeronautics and Space Administration Modern Era Retrospective-Analysis for Research and Applications (MERRA) [*Rienecker et al.*, 2011], the National Oceanic and Atmospheric Administration Climate Forecast System Reanalysis (CFSR), and the Japanese 55 year Reanalysis (JRA-55) [*Kobayashi et al.*, 2015]. These reanalysis data start at 1979, except for CRU and JRA-55, which start at 1901 and 1958, respectively, and have been continually updated to the present day. Further details of these data, such as their resolution, can be found in Table 1.

Notably, snow data from the above four sets of reanalysis data were respectively combined with CRU air temperature; they were named as CRU_ERA-Interim, CRU_MERRA, CRU_CFSR, and CRU_JRA-55. Together with four stand-alone sets of reanalysis data, these four combined sets of reanalysis data were used to drive the SFI model.

The historical and future climate data used to drive the SFI model were obtained from CMIP5 simulations. These data include monthly surface air temperature, snow depth, and snow mass (used to calculate snow density). Four RCPs were used: RCP2.6, RCP4.5, RCP6.0, and RCP8.5. Climate model releasing data on all three variables above required by the SFI model as forcing data were selected; otherwise, they was eliminated. Accordingly, 15, 21, 12, and 22 models (corresponding model names were shown in Table 1) were selected for RCP2.6, RCP4.5, RCP6.0, and RCP8.5, respectively. For each model, the same data sets (surface air temperature, snow depth, and snow mass) were employed to drive the SFI model. Because there was at least an element

Table 1. Details of the Models and Data[a]

Model Name	Resolution (°lon × °lat)	Air Temperature (°C)	Winter Snow Depth (m)	RCP2.6 (15 Models)	RCP4.5 (21 Models)	RCP6.0 (12 Models)	RCP8.5 (22 Models)	Model Reference
ACCESS1-0	1.3 × 1.9	-11.24	0.30		Y		Y	*Bi et al.* [2013]
bcc-csm1-1	2.8 × 2.8	-9.82	0.50	Y	Y		Y	*Wu et al.* [2010]
bcc-csm1-1-m	1.1 × 1.1	-9.08	0.53	Y	Y	Y	Y	*Wu et al.* [2010]
CanESM2	2.8 × 2.8	-8.77	0.26	Y	Y		Y	*Flato et al.* [2000]
CCSM4	0.9 × 1.3	-10.98	0.54	Y	Y	Y	Y	*Gent et al.* [2011]
CESM1-BGC	0.9 × 1.3	-10.89	0.54		Y		Y	*James et al.* [2013]
CESM1-CAM5	0.9 × 1.3	-13.07	0.49	Y	Y	Y	Y	*James et al.* [2013]
CMCC-CMS	1.9 × 1.9	-11.37	0.21		Y		Y	*Scoccimarro et al.* [2011]
CNRM-CM5	1.4 × 1.4	-11.78	0.39	Y	Y		Y	*Voldoire et al.* [2013]
CSIRO-Mk3.6.0	1.9 × 1.9	-11.87	0.22	Y	Y	Y	Y	*Jeffrey et al.* [2013]
GISS-E2-H	2.0 × 2.5	-9.17	0.38	Y	Y	Y	Y	*Schmidt et al.* [2014]
GISS-E2-H-CC	2.0 × 2.5	-9.50	0.38		Y		Y	*Schmidt et al.* [2014]
GISS-E2-R	2.0 × 2.5	-9.33	0.34	Y	Y	Y	Y	*Schmidt et al.* [2014]
GISS-E2-R-CC	2.0 × 2.5	-9.53	0.34		Y		Y	*Schmidt et al.* [2014]
INMCM4	1.5 × 2.0	-9.48	0.25		Y		Y	*Volodin et al.* [2010]
MIROC5	1.4 × 1.4	-9.88	0.34	Y	Y	Y	Y	*Watanabe et al.* [2010]
MIROC-ESM	2.8 × 2.8	-7.73	0.31	Y	Y	Y	Y	*Watanabe et al.* [2011]
MIROC-ESM-CHEM	2.8 × 2.8	-7.95	0.32	Y	Y	Y	Y	*Watanabe et al.* [2011]
MRI-CGCM3	1.1 × 1.1	-10.89	0.38	Y	Y	Y	Y	*Yukimoto et al.* [2012]
MRI-ESM1	1.1 × 1.1	-10.45	0.37				Y	*Yukimoto et al.* [2011]
NorESM1-M	1.9 × 2.5	-12.05	0.56	Y	Y	Y	Y	*Bentsen et al.* [2013]
NorESM1-ME	1.9 × 2.5	-13.03	0.59	Y	Y	Y	Y	*Tjiputra et al.* [2013]
ERA-Interim	0.7 × 0.7	-9.99	0.61					*Dee et al.* [2011]
MERRA	0.5 × 0.7	-9.52	0.34					*Rienecker et al.* [2011]
CFSR	0.3 × 0.3	-9.53	0.46					*Saha et al.* [2010]
JRA-55	1.1 × 1.1	-9.46	0.33					*Kobayashi et al.* [2015]
CRU	0.5 × 0.5	-10.77						*Harris et al.* [2014]

[a]Air temperature and winter snow depth are area-averaged values over the simulated present-day permafrost area. The letter "Y" means the model which was used in the corresponding RCP scenario.

(e.g., submodel, physical scheme, or resolution) that is different between these climate models, it was assumed that the simulated data from each climate model were statistically independent. Details of which models were selected for which RCP, along with further key information, are provided in Table 1. The CMIP5 simulations are usually initialized with multicentury preindustrial control (quasi-equilibrium) integrations [*Taylor et al.*, 2012]. Additional details regarding the simulations can be found in *Taylor et al.* [2012]. The data are archived at the website of the Earth System Grid Federation gateway (http://pcmdi9.llnl.gov/esgf-web-fe/). These data have been used worldwide in research on the causes of recent global climate warming and projections of future climate change [*Collins et al.*, 2013; *Chen et al.*, 2014; *Liu and Jiang*, 2016a, 2016b].

The International Permafrost Association (IPA) map, which is perhaps the best available data on the distribution of permafrost, was used as observations of permafrost distribution to validate the simulated results [*Brown et al.*, 1997]. The data are archived in a gridded format at a horizontal resolution of 0.5° longitude × 0.5° latitude at the following website: http://nsidc.org/data/docs/fgdc/ggd318_map_circumarctic/index.html. The data provided information on continuous, discontinuous, isolated, and sporadic permafrost and glaciers. Because it is believed that the model can only capture continuous and discontinuous permafrost [*Burn and Nelson*, 2006], these two types of permafrost were extracted to carry out the comparisons. The glacier data were used as a mask to exclude areas underlain by glaciers. In addition, in this study, the horizontal resolution of the IPA map was taken as a benchmark; all data, including both the reanalysis data and the climate model data, were interpolated into a common resolution of 0.5° longitude × 0.5° latitude for homogenous comparison.

2.3. Methods

Mean surface air temperatures of the warmest and coldest months required by the SFI model were directly calculated using monthly air temperature data from the climate model. When calculating the mean winter snow depth and snow density, a weighted mean was performed with monthly surface air temperature below 0°C. This method can obtain more meaningful mean winter snow data for expressing the effect of snow insulation, as compared to the arithmetic mean. This is because the latter uses the original seasonal asymmetric snow depth and snow density resulting from the accumulation of snow. More details are available in *Slater and Lawrence* [2013].

To remove any systematic biases in the climatic variables of the climate models, yearly anomalies of each variable, relative to the 1986–2005 average, were first calculated, and these anomalies were then added to the averages of the reanalysis data for 1986–2005. For surface air temperatures, the anomalies refer to a change, but for snow depth and snow density, they refer to a proportional change. This method has been successfully applied to correct systematic biases of a climate model [*Yan et al.*, 2014], but it is underpinned by an assumption that these biases do not change with time.

Absolute area bias (AAB) and bias were used to evaluate the consistency between the simulated and observed permafrost areas. The former was defined as the sum of the area of disagreeing grid boxes between two permafrost distributions. The latter means the difference in areas of two permafrost distributions. AAB may be a strict target, but it can reflect the actual deviation of two permafrost areas.

3. Results

3.1. Reanalysis Data Choice and Model Validation

Because the projection of permafrost used reanalysis data climatology that was added to by the climatic anomalies from the climate models, an accurate reanalysis data climatology was fundamentally important for the projection. Therefore, we first investigated the sensitivity of the SFI model to different reanalysis data to select a set of appropriate reanalysis data before carrying out the projection of permafrost.

As shown in Figures 1a–1h, all of the simulated permafrost extents from each set of reanalysis data generally fit well with the observed extent. However, more specifically, a common shortcoming is apparent in that the simulation tends to overestimate the Labradorean permafrost area in northeastern Canada and underestimate the permafrost areas in southern Alaska, United States, and in the northern Western Siberian Plain, Russia. The AABs of the eight sets of reanalysis data range from 4.9 to 7.2×10^6 km^2. The permafrost area from CFSR shows the largest AAB with observations, while the area from CRU_CFSR shows the smallest AAB. Notably, the simulated result is an average during the period 1998–2005, due to the lack of data, while the observations were developed using the data derived from 1960 to 1993. Some changes in permafrost extent may have occurred via these two periods. Therefore, when one discerns these AABs, period mismatch in the comparison needs to be kept in mind. Despite this issue, the CRU_CFSR data were selected to serve the projection because it has the smallest AAB.

As shown in Figure 2a, the SFI model, driven by the CRU_CFSR climatology plus ensemble mean anomalies of multiple models, yields a present-day (1986–2005 average) ensemble mean permafrost area of 15.45×10^6 km^2, which is quite close to the area of 15.24×10^6 km^2 from observations, with a bias and AAB of 0.21 and 4.7×10^6 km^2, respectively. In this study, this area is taken as the "simulated present-day permafrost area." Considering the aforementioned mismatch in period in this comparison (average over 1986–2005 for the simulation versus the period 1960–1993 for the observation), these results indicate that the model can reasonably reproduce the permafrost extent in the Northern Hemisphere.

The different simulated present-day permafrost areas from 20 climate models (all climate models shown in Table 1, but except for CMCC-CMS and GISS-E2-R-CC due to the lack of historical data) are shown in Figure 2b. All of the climate models capture a common permafrost area of 14.22×10^6 km^2, which occupies 93% of the total observed area of 15.24×10^6 km^2. The differences between the permafrost areas from the climate models are small, with a range from 0 to 2.81×10^6 km^2, mostly distributed at the edges of the permafrost region. Thus, all of the climate models were used in the projection.

3.2. Comparison of Future High-Latitude and High-Altitude Permafrost Degradation

The Tibetan Plateau is a typical and major high-altitude permafrost region in the Northern Hemisphere. Thus, in this study, we used the permafrost of the Tibetan Plateau to represent high-altitude permafrost and the permafrost outside the Tibetan Plateau as high-latitude permafrost.

Figures 3a–3b indicate that, despite the differences between individual climate models, changes in simulated ensemble mean air temperature fit well with that in the CRU data during the historical period from 1986 to 2005, with correlation coefficients of 0.54 and 0.74 for high-latitude and high-altitude permafrost areas, respectively, all with statistical significance exceeding 95%. By 2099, the ensemble mean air temperature will

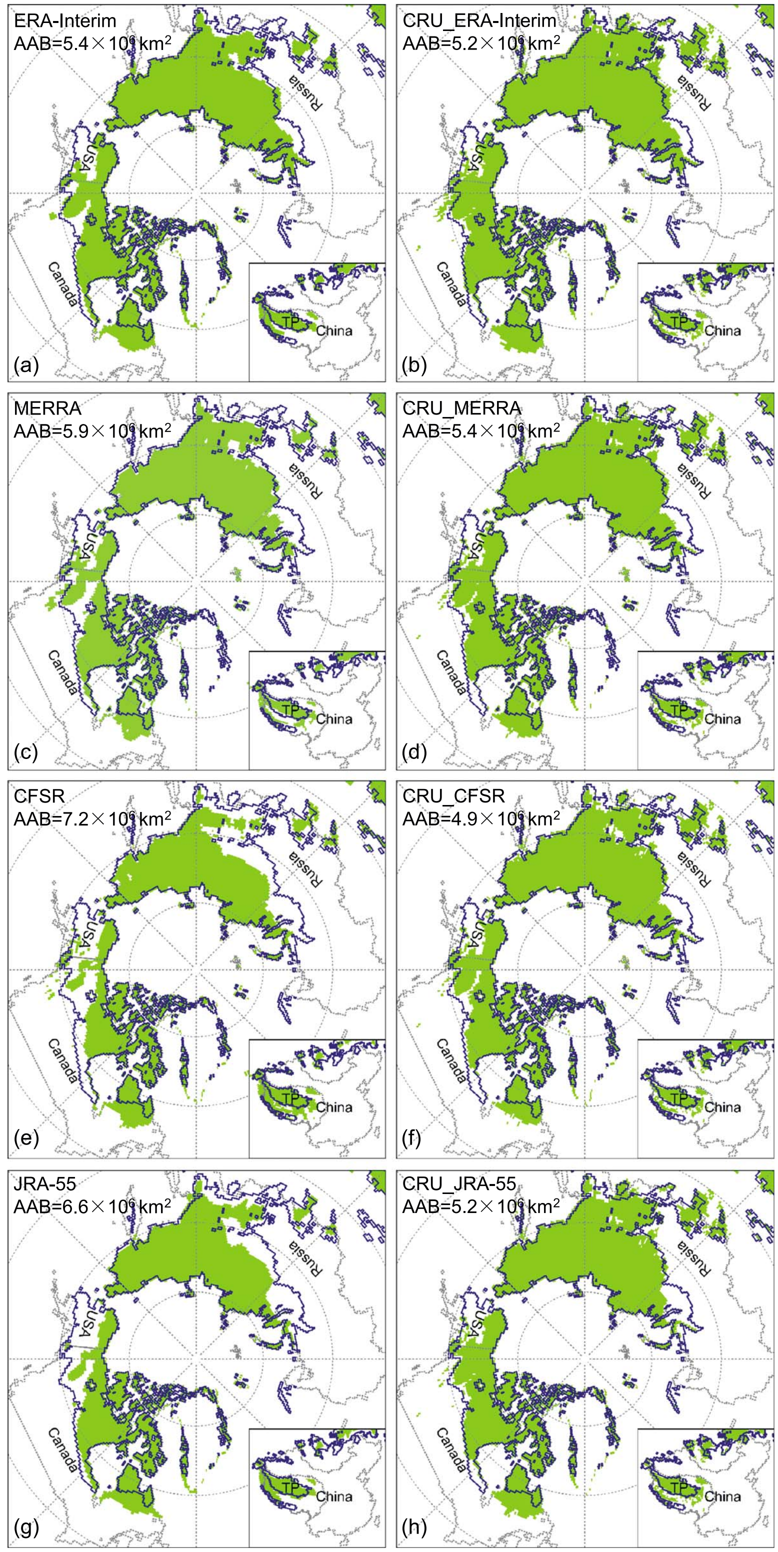

Figure 1. Comparison of the simulated (green areas) and observed (areas outlined in blue) permafrost areas. The simulated permafrost areas were diagnosed by the SFI model driven by (a) ERA-Interim, (c) MERRA, (e) CFSR, (g) JRA-55, (b) CRU_ERA-Interim, (d) CRU_MERRA, (f) CRU_CFSR, and (h) CRU_JRA-55 data, which were averages during the period from 1998 to 2005. The name of reanalysis data used and the AAB between the simulated and observed permafrost areas are given in the top left corner of each panel. Four countries and the Tibetan Plateau (TP), containing mostly permafrost, are indicated by the gray dashed lines.

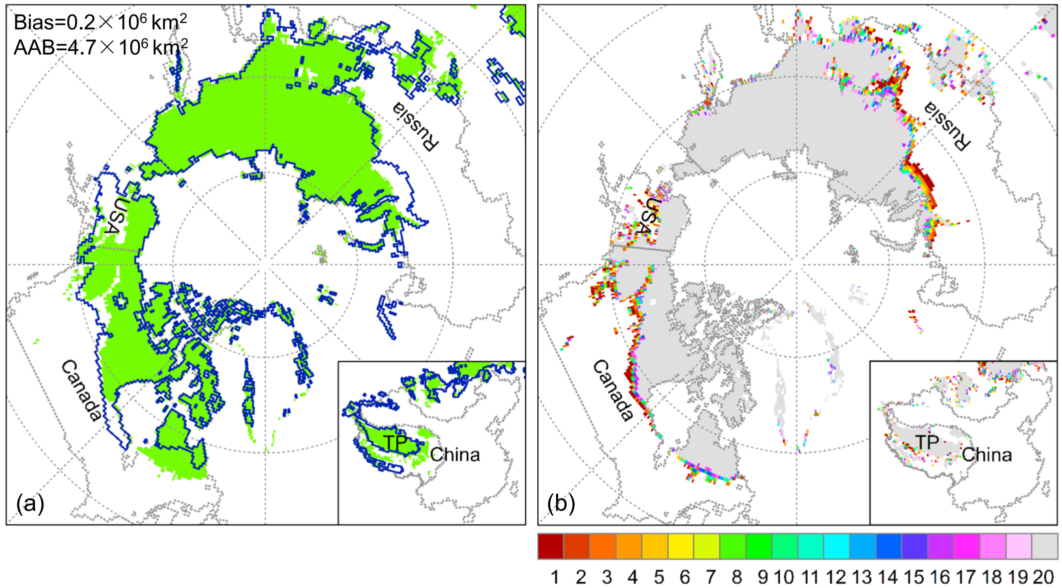

Figure 2. (a) Comparison of the simulated (green area) and observed (areas outlined in blue) present-day permafrost areas and (b) differentiation of the simulated present-day (1986–2005 average) permafrost areas from 20 climate models. In Figure 2a, the simulated permafrost area has been diagnosed by the SFI model driven by the CRU_CFSR data climatology plus ensemble mean anomalies of multimodels. Bias and the AAB between simulated and observed permafrost areas are given in the top left corner of the panel. In Figure 2b, the simulated permafrost area has been diagnosed by the SFI model driven by the CRU_CFSR data climatology plus anomalies of each model. The unit of the color bar is the total number of models that captured the same permafrost area. Four countries and the Tibetan Plateau (TP), containing mostly permafrost, are indicated by the gray dashed lines.

increase by 2.3°C (RCP2.6), 3.8°C (RCP4.5), 5.0°C (RCP6.0), and 8.0°C (RCP8.5) over the high-latitude permafrost area, which is higher than the values of 1.5°C (RCP2.6), 2.9°C (RCP4.5), 3.9°C (RCP6.0), and 6.0°C (RCP8.5) over the high-altitude permafrost area. Trends in air temperatures during the near term (2006–2035) and long term (2006–2009) under the four RCPs are also given, in Figures 4a–4b. The higher RCPs appear to produce a larger trend in air temperature for the long term but, for the near term, RCP6.0 has the smallest means for trends in air temperature across the climate models. For RCP6.0 and RCP8.5, the long-term trends appear to be larger than the near term but, for RCP2.6 and RCP4.5, the long-term trends appear to be smaller than the near term. The high-latitude permafrost region appears to show a higher trend in air temperature than the high-altitude permafrost region in corresponding RCPs and periods.

In response to the above warming in air temperature, both the high-latitude and high-altitude permafrost areas show a significant decrease during the historical and future periods (Figure 5). For the historical period, a decreasing 8 year series of permafrost area from CRU_CFSR data is similar to that from the ensemble mean of the climate

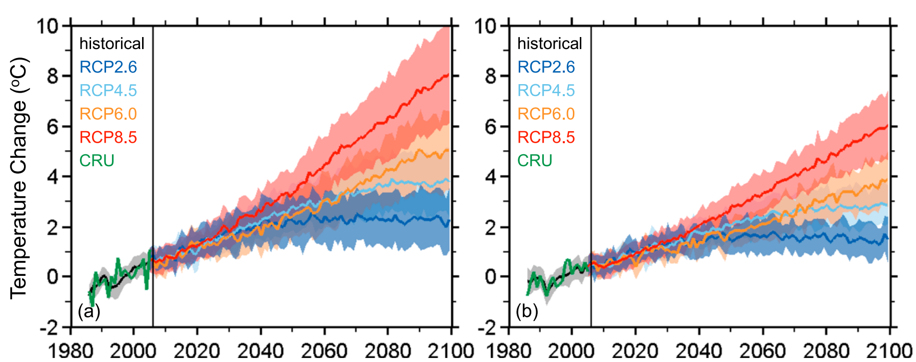

Figure 3. Area-averaged changes in surface air temperature as averaged over the simulated present-day (a) high-latitude and (b) high-altitude permafrost areas during the period from 1986 to 2099, relative to the period 1986–2005. Shaded areas represent one standard deviation across models.

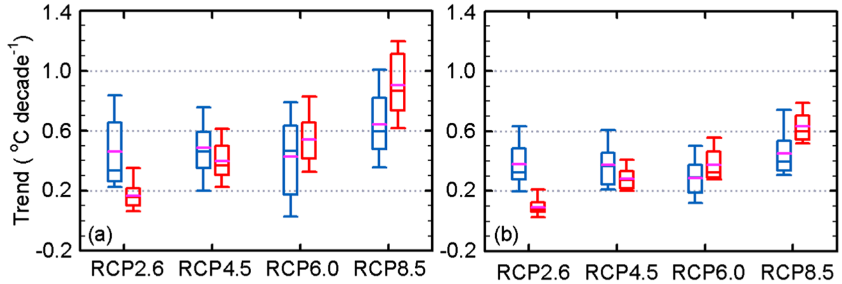

Figure 4. Area-averaged trends in surface air temperature as averaged over the simulated present-day (a) high-latitude and (b) high-altitude permafrost areas during the near term (2006–2035) (blue boxplot) and long term (2006–2099) (red boxplot) under four RCP scenarios. Box-and-whisker plots indicate 10th and 90th percentiles (whiskers), 25th and 75th percentiles (box ends), the median (solid middle line colored the same as the corresponding boxplot), and means (pink solid middle line).

models for the two kinds of permafrost, especially high-altitude permafrost (Figures 5a and 5c). Under RCP2.6 and RCP4.5, the permafrost areas decline at first but appear to gradually become more stable near 2099. However, under RCP6.0 and RCP8.5, the permafrost areas continually decline until 2099. By 2099, the remaining ensemble mean permafrost area will be 68% (RCP2.6), 51% (RCP4.5), 42% (RCP6.0), and 21% (RCP8.5) over the high-latitude permafrost area but will be 55% (RCP2.6), 31% (RCP4.5), 22% (RCP6.0), and 3% (RCP8.5) over the high-altitude permafrost area, albeit with a wide range existing across the climate models (Figures 5b and 5d).

In order to compare the speed of permafrost thaw in different regions, percentage (relative to the 1986–2005 period) trends in permafrost area were calculated (Figures 6a–6d). The percentage trends in the high-altitude permafrost area appear to be larger than those in the high-latitude area—not only under every RCP but also during every period (near term and long term), indicating a faster thaw of high-altitude permafrost than that of high-latitude permafrost. For both high-latitude and high-altitude permafrost, the percentage trend during the near term is larger than that during the long term under all RCPs except for RCP8.5, indicating that under RCP2.6, RCP4.5, and RCP6.0, permafrost thaw during the near term is faster than that during the long term.

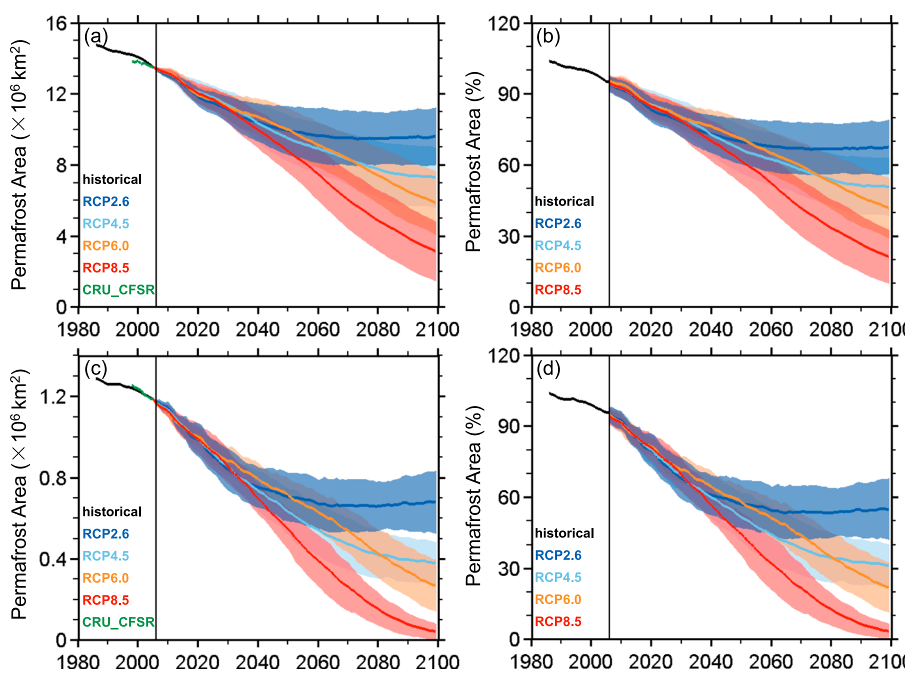

Figure 5. Projected changes in (a, b) high-latitude and (c, d) high-altitude permafrost areas during the period from 1986 to 2099. Figures 5a and 5c refer to absolute permafrost area, while Figures 5b and 5d refer to the percentage of permafrost area relative to the 1986–2005 period. Shaded areas represent one standard deviation across models. The green line represents change in the permafrost area diagnosed by the SFI model driven by the CRU_CFSR data.

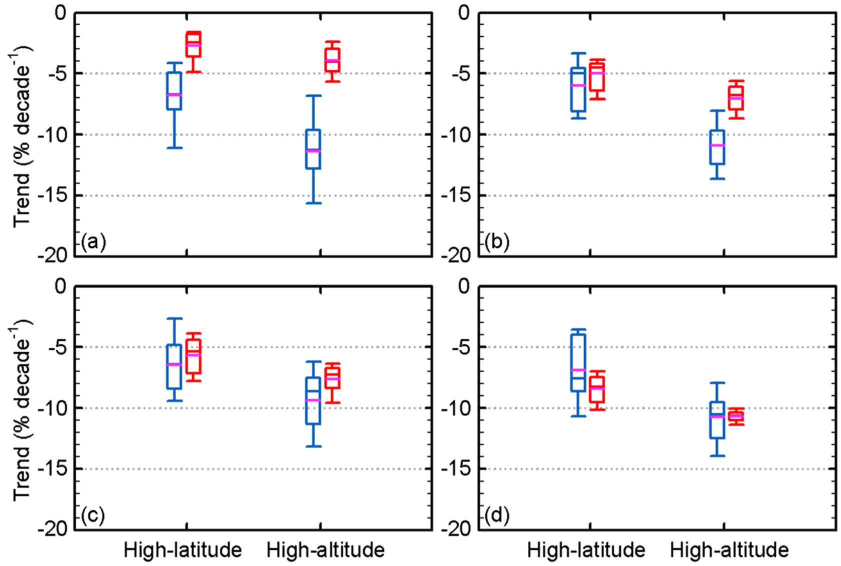

Figure 6. Projected percentage trends in high-latitude and high-altitude permafrost areas during the near term (2006–2035) (blue boxplot) and long term (2006–2099) (red boxplot) under the (a) RCP2.6, (b) RCP4.5, (c) RCP6.0, and (d) RCP8.5 scenarios. The explanation of the box-and-whiskers plots is the same as in Figure 4.

Notably, the larger percentage trends in the high-altitude permafrost area than those in the high-latitude permafrost area do not mean that high-altitude permafrost thaw more, in terms of absolute amount, than high-latitude permafrost during a particular period due to significantly smaller present-day high-altitude permafrost area (1.24×10^6 km^2, this study) than high-latitude permafrost area (14.22×10^6 km^2, this study).

The larger percentage trend of the high-altitude than high-latitude permafrost area can be explained well by the larger percentage sensitivity of the high-altitude permafrost than that of the high-latitude permafrost to rising air temperature, as illustrated in Figure 7. As shown in Figures 7a–7d, the percentage sensitivities of ensemble mean high-altitude permafrost area to air temperature change are $-33\%°C^{-1}$ (RCP2.6), $-26\%°C^{-1}$ (RCP4.5), $-20\%°C^{-1}$ (RCP6.0), and $-17\%°C^{-1}$ (RCP8.5), which are much larger than the values of $-16\%°C^{-1}$ (RCP2.6), $-13\%°C^{-1}$ (RCP4.5), $-11\%°C^{-1}$ (RCP6.0), and $-10\%°C^{-1}$ (RCP8.5) for the high-latitude permafrost. In spite of this fact, in contrast, the air temperature in the high-altitude permafrost region shows a lower trend than those in the high-latitude permafrost region (Figures 4a and 4b) (Table 2). This indicates that the percentage permafrost sensitivity to rising air temperature is perhaps the dominant factor affecting the percentage trend of permafrost area.

The differences in percentage sensitivity of high-altitude and high-latitude permafrost to rising air temperature are likely related to their thermal conditions. Firstly, ERA-Interim soil temperature at 1 m depth shows that, on area average, the high-altitude permafrost is 6.77°C warmer than the high-latitude permafrost (Figure 8). Additionally, according to the definition of permafrost, permafrost is identified as whether the ground remains at or below 0°C continuously for at least 2 years. If ground temperature rises the same degree for both warm and cold permafrost, the warm permafrost more easily exceeds 0°C and becomes nonpermafrost than the cold permafrost, thus resulting in a larger percentage sensitivity of the warm permafrost than the cold permafrost to rising air temperature.

3.3. Comparison of Future Degradation of Permafrost in Different Countries

Because continuous and discontinuous permafrost are mostly distributed in Russia, Canada, the United States, and China, projections of permafrost in these four countries and comparison between them were carried out and are reported in this section. Notably, for the different countries, the simulated results from the same climate models were used for comparison.

Figures 9a–9d show the area-averaged changes in air temperature over the present-day permafrost area in the four countries. During the historical period, air temperatures in all four countries experienced significant

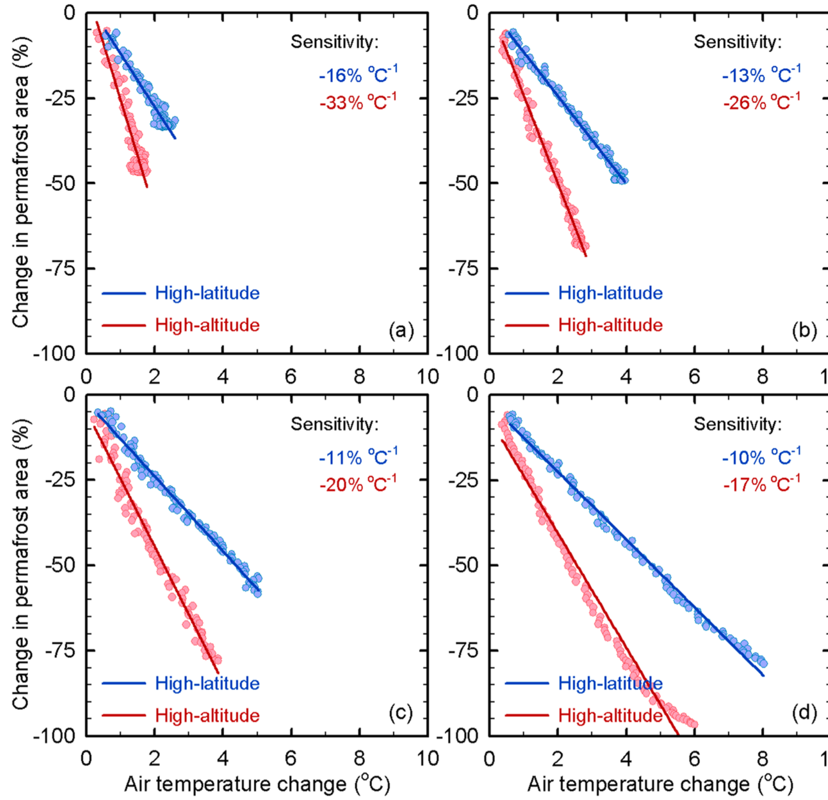

Figure 7. Percentage sensitivities of ensemble mean high-latitude and high-altitude permafrost areas to area-averaged changes in surface air temperature as averaged over the simulated present-day high-latitude and high-altitude permafrost areas under the (a) RCP2.6, (b) RCP4.5, (c) RCP6.0, and (d) RCP8.5 scenarios. The solid lines represent linear fits.

Table 2. Statistics of Surface Air Temperature Trend (°C Decade^{-1}) and Percentage Permafrost Area Trend (% Decade^{-1}) of Each Model for High-Latitude and High-Altitude Permafrost During the Period From 2006 to 2099 Under the RCP4.5 Scenario

	High-Latitude Permafrost		High-Altitude Permafrost	
Model Name	Temperature Trend	Percentage Permafrost Area Trend	Temperature Trend	Percentage Permafrost Area Trend
ACCESS1-0	0.41	-5.15	0.36	-7.75
bcc-csm1-1	0.34	-4.31	0.20	-5.75
bcc-csm1-1-m	0.30	-4.39	0.18	-5.55
CanESM2	0.44	-6.09	0.31	-6.77
CCSM4	0.31	-4.26	0.20	-6.05
CESM1-BGC	0.29	-4.62	0.21	-5.76
CESM1-CAM5	0.52	-7.19	0.34	-8.30
CMCC-CMS	0.44		0.33	
CNRM-CM5	0.42	-4.22	0.25	-5.49
CSIRO-Mk3.6.0	0.33	-4.22	0.31	-7.71
GISS-E2-H	0.27	-3.89	0.31	-8.56
GISS-E2-H-CC	0.27	-3.84	0.27	-6.73
GISS-E2-R	0.14	-2.55	0.22	-6.88
GISS-E2-R-CC	0.12		0.23	
INMCM4	0.29	-4.07	0.23	-6.11
MIROC5	0.63	-4.53	0.43	-7.99
MIROC-ESM	0.41	-7.22	0.39	-9.16
MIROC-ESM-CHEM	0.60	-6.66	0.43	-8.73
MRI-CGCM3	0.33	-4.49	0.21	-6.37
NorESM1-M	0.48	-6.53	0.24	-6.77
MorESM1-ME	0.49	-6.93	0.30	-7.63
Ensemble mean	0.37	-5.01	0.28	-7.05

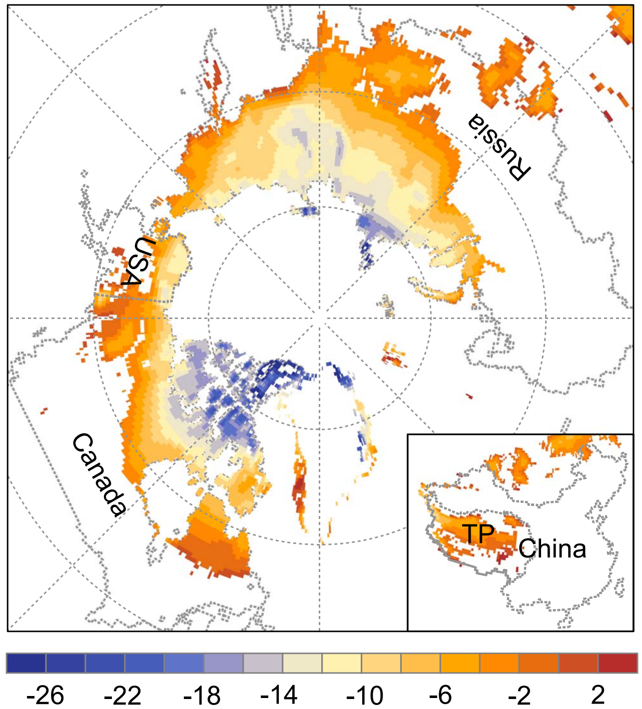

Figure 8. Distribution of ERA-Interim soil temperature (°C) at 1 m depth in the present-day permafrost area, which is an average over the period from 1986 to 2005. Area-averaged soil temperatures are −9.26 and −2.49°C for high-latitude and high-altitude permafrost areas and are −8.61, −10.30, −6.54, and −2.39°C for permafrost areas in Russia, Canada, the United States, and China. Four countries and the Tibetan Plateau (TP), containing mostly permafrost, are indicated by the gray dashed lines.

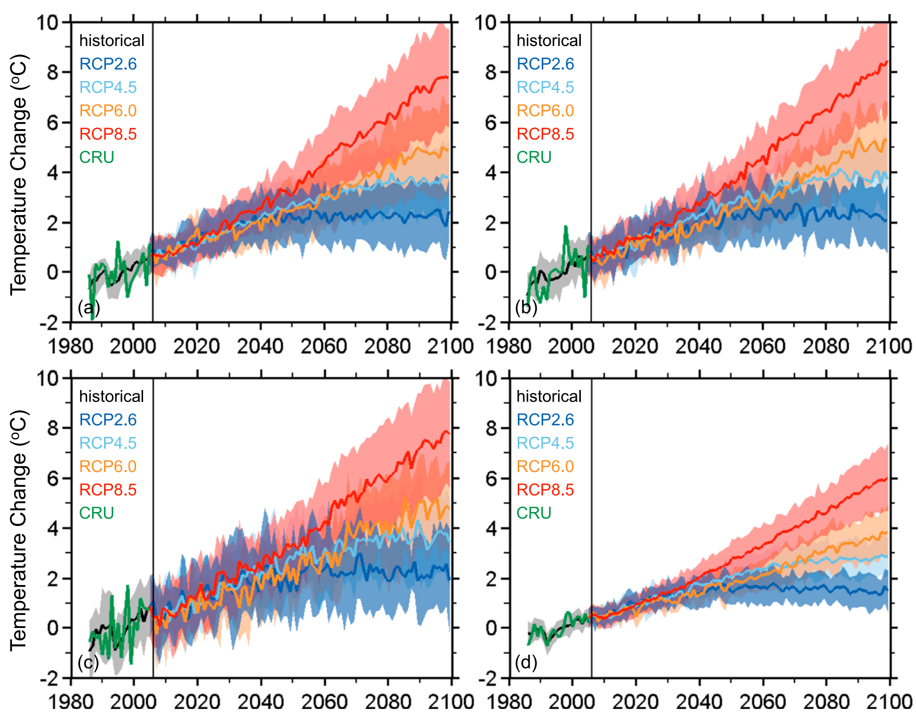

Figure 9. Area-averaged changes in surface air temperature as averaged over the simulated present-day permafrost areas in (a) Russia, (b) Canada, (c) the United States, and (d) China during the period from 1986 to 2099. Shaded areas represent one standard deviation across models.

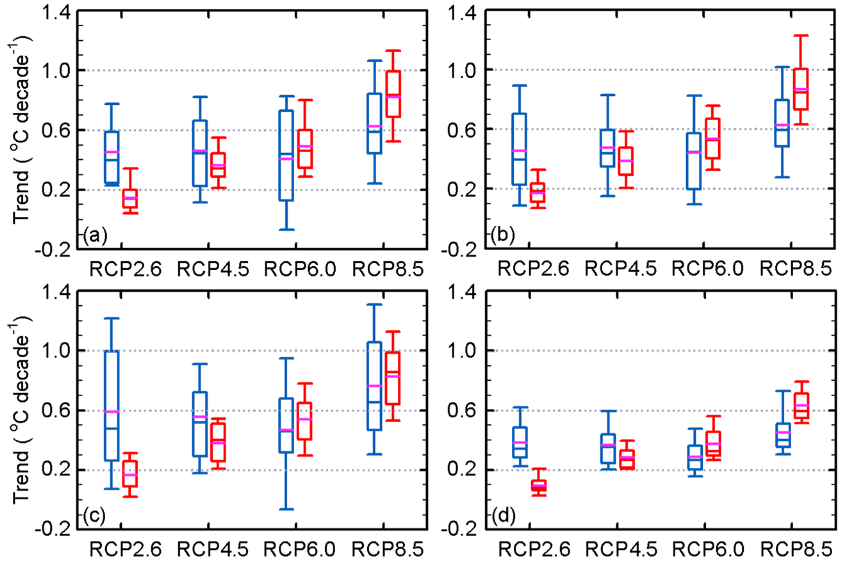

Figure 10. Area-averaged trends in surface air temperature as averaged over the simulated present-day permafrost areas in (a) Russia, (b) Canada, (c) the United States, and (d) China during the near term (2006–2035) (blue boxplot) and long term (2006–2099) (red boxplot) under four RCP scenarios. The explanation of the box-and-whiskers plots is the same as in Figure 4.

increases; the ensemble mean series are similar to the series of CRU data, with correlation coefficients of 0.24, 0.44, 0.41, and 0.77 for Russia, Canada, the United States, and China, respectively, all with statistical significance exceeding 90% except for Russia. During the future period, these increases will continue and the ensemble mean values are 2.4, 3.8, 4.9, and 7.7°C for Russia; 2.1, 3.7, 5.3, and 8.4°C for Canada; 1.9, 3.4, 4.8, and 7.7°C for the United States; and 1.5, 2.9, 3.8, and 6.0°C for China under RCP2.6, RCP4.5, RCP6.0, and

Table 3. Statistics of Surface Air Temperature Trend (°C Decade^{-1}) and Percentage Permafrost Area Trend (% Decade^{-1}) of Each Model for Permafrost in Russia, Canada, the United States, and China During the Period From 2006 to 2099 Under the RCP4.5 Scenario

	Russia		Canada		United States		China	
Model Name	Temperature Trend	Percentage Permafrost Area Trend	Temperature Trend	Percentage Permafrost Area Trend	Temperature Trend	Percentage Permafrost Area Trend	Temperature Trend	Percentage Permafrost Area Trend
ACCESS1-0	0.37	-5.21	0.48	-5.09	0.46	-7.91	0.35	-7.55
bcc-csm1.1	0.34	-4.58	0.34	-3.81	0.40	-4.68	0.20	-5.85
bcc-csm1.1.m	0.26	-4.06	0.37	-4.65	0.26	-8.73	0.19	-5.67
CanESM2	0.42	-6.91	0.48	-4.84	0.40	-6.93	0.31	-6.89
CCSM4	0.33	-5.05	0.27	-3.23	0.27	-3.95	0.21	-5.94
CESM1-BGC	0.31	-4.46	0.26	-5.07	0.24	-6.54	0.22	-6.00
CESM1-CAM5	0.47	-7.57	0.58	-6.62	0.57	-11.01	0.33	-8.34
CMCC-CMS	0.43		0.43		0.51		0.32	
CNRM-CM5	0.41	-3.87	0.42	-4.67	0.35	-6.59	0.25	-5.52
CSIRO-Mk3-6-0	0.29	-4.10	0.39	-4.15	0.51	-8.45	0.30	-7.95
GISS-E2-H	0.24	-4.43	0.30	-3.23	0.24	-3.33	0.29	-8.34
GISS-E2-H-CC	0.24	-3.41	0.31	-4.46	0.23	-5.48	0.26	-6.76
GISS-E2-R	0.16	-3.00	0.10	-1.85	0.16	-3.53	0.21	-6.69
GISS-E2-R-CC	0.12		0.11		0.14		0.22	
Inmcm4	0.31	-4.10	0.27	-3.98	0.28	-6.05	0.22	-6.38
MIROC5	0.63	-4.68	0.61	-4.36	0.64	-4.70	0.43	-7.90
MIROC-ESM	0.37	-7.46	0.45	-6.70	0.40	-10.01	0.38	-9.05
MIROC-ESM-CHEM	0.62	-7.13	0.59	-5.86	0.52	-8.21	0.42	-8.48
MRI-CGCM3	0.31	-4.83	0.35	-3.67	0.32	-5.18	0.21	-6.98
NorESM1-M	0.50	-7.40	0.46	-5.34	0.49	-6.70	0.25	-6.89
NorESM1-ME	0.47	-7.45	0.53	-6.45	0.53	-9.45	0.30	-7.47
Ensemble mean	0.36	-5.25	0.39	-4.63	0.38	-6.71	0.28	-7.09

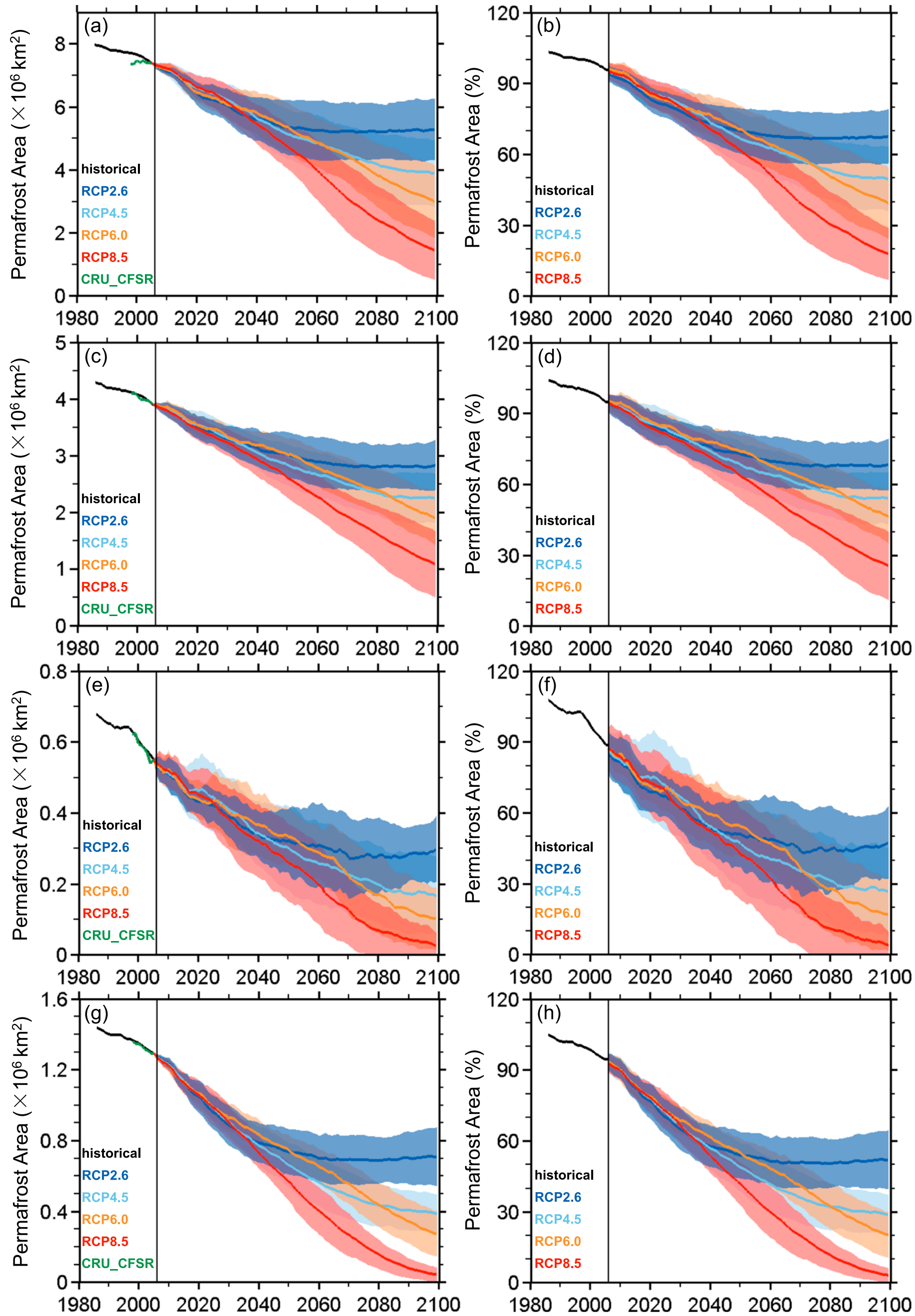

Figure 11. Projected changes in permafrost areas in (a, b) Russia, (c, d) Canada, the (e, f) United States, and (g, h) China during the period from 1986 to 2099. Figures 11a, 11c, 11e and 11g refer to absolute permafrost area, while Figures 11b, 11d, 11f, and 11h refer to the percentage of permafrost area relative to the 1986–2005 period. Shaded areas represent one standard deviation across models. The green line represents change in permafrost area diagnosed by the SFI model driven by the CRU_CFSR data.

RCP8.5, respectively, by 2099. As shown in Figures 10a–10d, for the long term, the trends of air temperature appear to increase along with the RCP ranging from 2.6 to 8.5 but, for the near term, this positive linear relationship is not apparent. Despite a large range across the models, the mean trends of air temperature in the long term are more similar between Russia, Canada, and the United States for corresponding RCPs. The trends of air temperature in China are much smaller than those in the other three countries. For instance, under RCP4.5, the mean trends in air temperature are 0.36, 0.39, and 0.38°C for Russia, Canada, and the United States, but 0.28°C for China (Table 3).

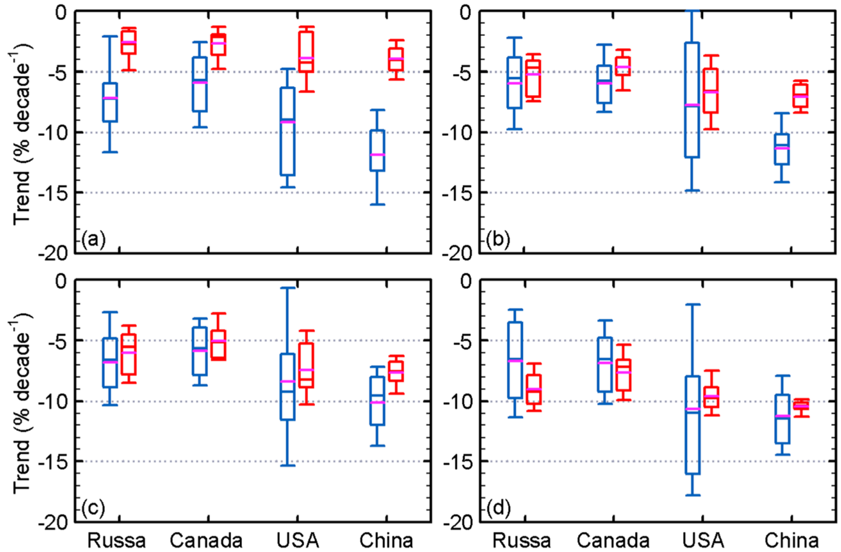

Figure 12. Projected percentage trends in permafrost areas in Russia, Canada, the United States, and China during the near term (2006–2035) (blue boxplot) and long term (2006–2099) (red boxplot) under the (a) RCP2.6, (b) RCP4.5, (c) RCP6.0, and (d) RCP8.5 scenarios. The explanation of the box-and-whiskers plots is the same as in Figure 4.

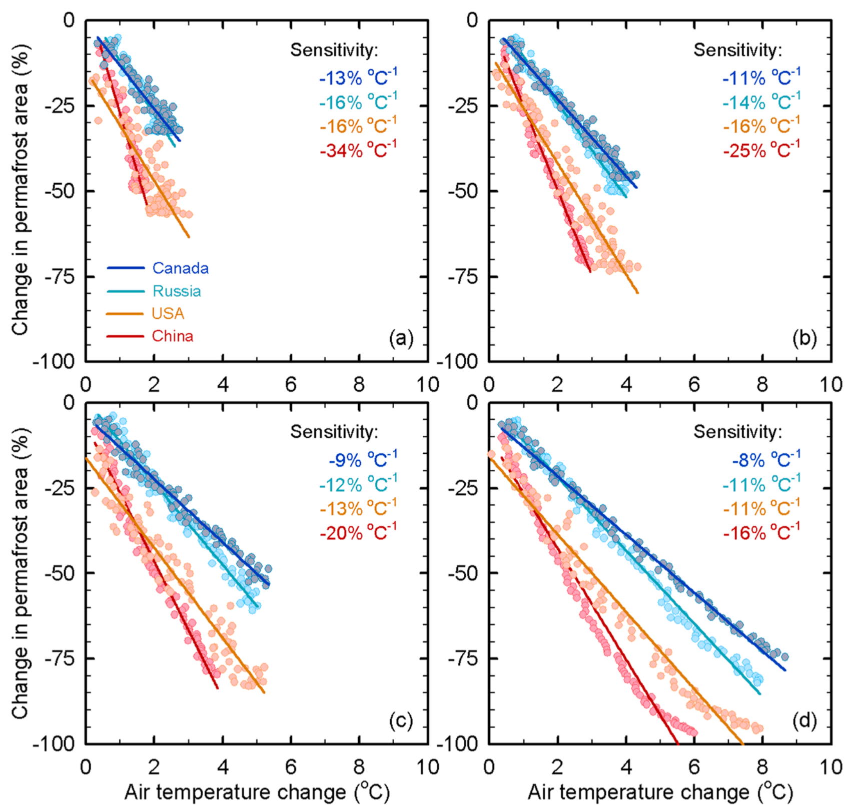

Figure 13. Percentage sensitivities of ensemble mean permafrost areas in Russia, Canada, the United States, and China to area-averaged changes in surface air temperature as averaged over the simulated present-day permafrost areas in the corresponding countries under the (a) RCP2.6, (b) RCP4.5, (c) RCP6.0, and (d) RCP8.5 scenarios. The solid lines represent linear fits.

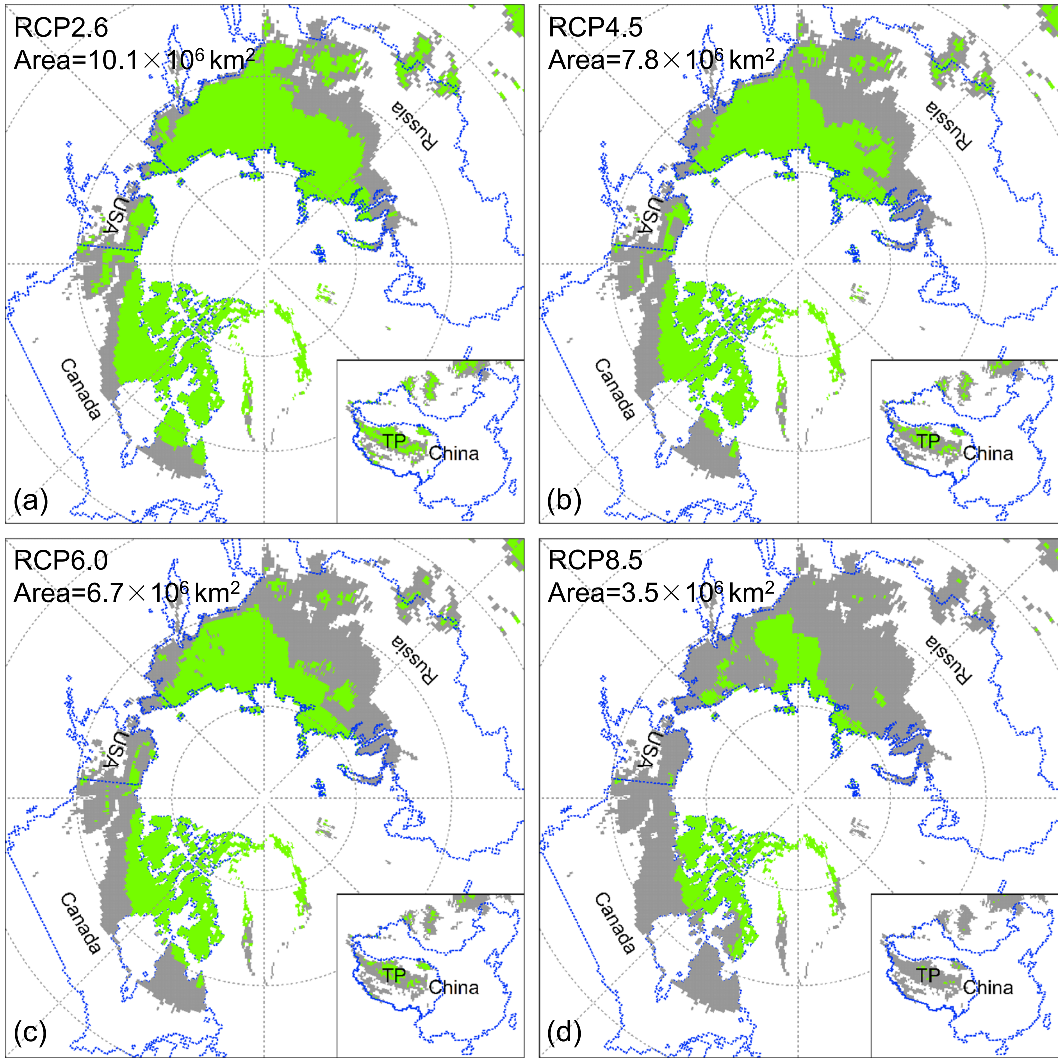

Figure 14. Projected ensemble mean permafrost area (green areas) during the period from 1980 to 2099 under four RCP scenarios. The gray area represents the simulated present-day permafrost area. The RCP scenario and area during the period from 1980 to 2099 are given in the top left corner of each panel. Four countries and the Tibetan Plateau (TP), containing mostly permafrost, are indicated by the blue dashed lines.

The changes in permafrost areas in the four countries during the historical and future periods are presented in Figure 11. During the historical period, the ensemble mean permafrost areas experience a significant decrease, which fits well with the results from CRU, except for the area in Russia (Figures 11a, 11c, 11e, and 11g). In Russia, the permafrost area from CRU is somewhat lower than the mean result from the climate models (Figure 11a). It is found that the results based on CRU data underestimate more permafrost in the northern Western Siberian Plain of Russia than that based on the climate models (not shown), which means that the results from the climate models are closer to reality than those from CRU data for the permafrost in Russia during the comparison period. This is also the reason for the relatively large deviation between the results from climate models and CRU for high-latitude permafrost, shown in Figure 5a. During the future period, the permafrost areas will continue to decrease and reach ensemble mean values of 68%, 50%, 39%, and 18% for Russia; 68%, 54%, 46%, and 26% for Canada; 47%, 27%, 17%, and 4% for the United States; and 52%, 29%, 20%, and 3% for China, under RCP2.6, RCP4.5, RCP6.0, and RCP8.5, respectively, by 2099 (Figures 11b, 11d, 11f, and 11h). It can be seen that some models indicate that no permafrost will remain in the United States by 2099, under RCP8.5.

Figures 12a–12d show the projected percentage (relative to the 1986–2005 period) trends in permafrost areas in the four countries during the near term and long term. Permafrost shows a faster thaw during the near term

Table 4. Projected Changes in Permafrost Area ($\times 10^6$ km^2 Decade^{-1}) During the Period From 2080 to 2099 Relative to the Period From 1986 to 2005 for High-Latitude and High-Altitude Permafrost and Permafrost in Russia, Canada, the United States, and China[a]

		2080–2099				Relative change			
	1986–2005	RCP2.6	RCP4.5	RCP6.0	RCP8.5	RCP2.6	RCP4.5	RCP6.0	RCP8.5
High latitude	14.21 ± 0.44	9.52 ± 1.51	7.45 ± 1.66	6.57 ± 1.71	3.96 ± 1.72	33% ± 11%	48% ± 12%	53% ± 12%	73% ± 12%
High altitude	1.24 ± 0.03	0.67 ± 0.13	0.40 ± 0.11	0.34 ± 0.12	0.09 ± 0.06	46% ± 11%	67% ± 9%	72% ± 10%	93% ± 4%
Russia	7.71 ± 0.26	5.24 ± 0.92	3.99 ± 1.04	3.39 ± 1.10	1.91 ± 0.99	32% ± 11%	49% ± 13%	55% ± 14%	76% ± 12%
Canada	4.12 ± 0.14	2.81 ± 0.39	2.27 ± 0.42	2.13 ± 0.42	1.34 ± 0.56	32% ± 9%	45% ± 10%	48% ± 10%	68% ± 13%
United States	0.63 ± 0.05	0.28 ± 0.08	0.18 ± 0.11	0.13 ± 0.09	0.05 ± 0.06	55% ± 14%	72% ± 18%	78% ± 16%	92% ± 8%
China	1.37 ± 0.04	0.70 ± 0.14	0.41 ± 0.11	0.35 ± 0.12	0.09 ± 0.06	49% ± 10%	70% ± 8%	74% ± 9%	93% ± 4%

[a]The range of uncertainty is one standard deviation across models.

than during the long term, except in Russia and Canada under the RCP8.5 scenarios. The trend in the United States shows a distinctly large uncertainty range during the near term, which could be related to the relatively small permafrost area in that country. During both the near term and long term, the permafrost area in China appears to show the fastest thaw among the four countries, with a percentage trend of -7.09% decade^{-1} during the long term under RCP4.5 scenario (Table 3). The permafrost area in the United States appears to show the second fastest thaw, with the percentage trend of -6.71% decade^{-1}, followed by Russia (the percentage trend: -5.25% decade^{-1}) and, lastly, Canada (the percentage trend: -4.63% decade^{-1}).

Such a discrepancy between the speeds of permafrost thaw in the four countries corresponds well to the discrepancy between the percentage sensitivities of ensemble mean permafrost area in the four countries to rising air temperature (Figure 13). As shown in Figures 13a–13d, the permafrost in China shows the largest percentage sensitivity, followed by that in the United States, Russia, and then Canada, under the four RCP scenarios. For instance, under RCP4.5, the percentage permafrost sensitivities are -25, -16, -14, and -11%°C^{-1} for China, the United States, Russia, and Canada, respectively. These results indicate that percentage permafrost sensitivities to rising air temperature are responsible for the speed of permafrost thaw in the four countries. Similar to the situation of high-altitude and high-latitude permafrost, the differences in percentage sensitivity of permafrost in these four countries to rising air temperature also are likely related to their thermal conditions (Figure 8). As shown in Figure 8, area-averaged soil temperatures at 1 m depth are -8.61°C, -10.30°C, -6.54°C, and -2.39°C for the permafrost region in Russia, Canada, the United States, and China, respectively, which correspond well to percentage sensitivities of permafrost in these four countries to rising air temperature.

The projected ensemble mean permafrost extents during the period 2080–2099 are presented in Figures 14a–14d. Under RCP2.6, RCP4.5, and RCP6.0, the degradation of permafrost in the different regions mainly occurs at the southern edge of the permafrost areas. Moreover, the permafrost gradually retreats toward the Arctic with the RCP increasing from 2.6 to 6.0. Under RCP8.5, there will be almost no permafrost in China, the United States, and the Tibetan Plateau by the period 2080–2099. Permafrost in Russia will remain mainly in the western part of the east Siberian Mountains, and permafrost in Canada will retreat to the north of approximately 65°N. Details of the remaining permafrost areas in different regions and their relative change against the present period of 1986–2005 are given in Table 4. By the period 2080–2099, permafrost areas will decrease by 48% and 67% for high-latitude and high-altitude permafrost, and by 49%, 45%, 72%, and 70% for Russia, Canada, the United States, and China under RCP4.5 on average, despite a wide range existing across the models. It should be stressed that these thaws of permafrost do not necessarily mean that permafrost in all soil layers will completely disappear; some deep permafrost might still remain in the regions where permafrost disappears, such as those shown in Figure 14.

4. Discussions

To understand in more depth the possible future changes in permafrost, a multiregion projection and comparison was carried out in this study using the SFI model and multimodel and multiscenario climate data from CMIP5 models. The results show that a severe thaw may occur for permafrost in all regions, but there are some different features of thaw (e.g., thaw amount and speed) shown for permafrost in different regions. In this section, we compare the present results with those from previous studies and analyze the potential sources of possible uncertainty.

4.1. Comparisons With Previous Results

Projected results from *Stendel and Christensen* [2002] and *Lawrence and Slater* [2005] showed significant poleward movement of permafrost extent in the Northern Hemisphere, and 60% and 90% decreases in the permafrost area by 2100 under the B1 and A2 scenarios. An 83% decrease in permafrost area north of 45°C by the period 1980–2099 under the A1B scenario was also given by *Lawrence et al*. [2008]. An improved study by *Lawrence et al*. [2012], based on CCSM4, showed that the total Northern Hemisphere area will decrease by 33% (RCP2.6), 49% (RCP4.5), 62% (RCP6.0), and 72% (RCP8.5) by the period 2080–2099, while the present study reports 34% ± 10% (RCP2.6), 49% ± 11% (RCP4.5), 55% ± 11% (RCP6.0), and 74% ± 11% (RCP8.5). Therefore, the present results are comparable to those from *Lawrence et al*. [2012], especially for the ensemble mean results, which are quite close to those from CCSM4.

Direct analysis of soil temperature outputs from the CMIP5 models shows that the permafrost area will decrease by 24% ± 45% (RCP2.6), 38% ± 44% (RCP4.5), and 65% ± 33% (RCP8.5) [*Koven et al*., 2013]. Compared to these previous results, the present results show a distinctly narrow range of projections and greater loss in the ensemble mean permafrost area by approximately 10%. The latter may be partially due to the greater permafrost sensitivity of the SFI model than direct soil temperature-based calculations to rising air temperature, as discussed in section 4.2. The present study shows a close to, but slightly lower, relative change than the results of *Slater and Lawrence* [2013]; the deviation between both results may be due to use of different reanalysis data and climate models.

A regional projection of permafrost on the Tibetan Plateau, carried out by *Guo et al*. [2012], reported an 81% decrease by the period 1980–2099 under the A1B scenario, while the present results indicate a value of 67% ± 9% under the RCP4.5 scenario, which is similar to A1B. Clearly, the present results are somewhat lower than those reported by *Guo et al*. [2012], which can largely be attributed to the different levels of increased air temperature in the two studies: 0.28 ± 0.07°C decade^{-1} and 0.58°C decade^{-1} for the present study and *Guo et al*. [2012], respectively, from 2006 to 2099.

4.2. Potential Sources of Possible Uncertainty

Although in this study systematic biases in climate data were removed through using climate anomalies added to the reanalysis data climatology, this method is based on an assumption that systematic biases of climate models do not change along with time. Therefore, those biases that do change along with time still exist as a source of possible uncertainty. Additionally, the horizontal resolution of the climate data is coarse, with a large range from 1.1° × 1.1° to 2.8° × 2.8°. This coarse resolution provides less regional information on climate change, which may to some extent prevent the model from capturing detailed change in permafrost, especially for the permafrost at the edge of the permafrost area. Such an effect on the simulation of permafrost may be magnified in the present projection of permafrost because of its regional focus.

When preparing the reanalysis data for use in this study, CRU air temperature and CFSR snow data were ultimately chosen. CRU data are constructed through the interpolation of station observations and are generally thought to be reliable, except for regions or periods with sparse observational data [*Harris et al*., 2014]. Compared with CRU air temperature, CFSR snow data may possess larger deviations because they are mostly based on modeling and assimilation [*Saha et al*., 2010]. The deviations in CFSR snow data could also be regarded as another source of possible uncertainty, though snow data could be less responsible for the biases in the simulation of permafrost than air temperature.

Slater and Lawrence [2013] indicated that the model shows an approximately 25% larger permafrost sensitivity to rising air temperature than raw diagnoses using soil temperature from the climate models. Such higher sensitivity may contribute to at least some of the uncertainties in the present permafrost simulation. Additionally, *Nelson and Outcalt* [1987] indicated that the SFI model is restricted to mapping a permafrost area covering less than about 0.5×10^6 km^2. In this study, the permafrost area of each regions is larger than this limited area. However, it should be mentioned that the permafrost area in the United States is relatively close to this limit, and thus, there is a larger uncertainty range shown in its results. In addition to these mentioned possible sources of uncertainty, some other sources may still exist in the present study.

5. Summary

Regional differences of future permafrost degradation were explored using the SFI model in combination with climatic change from CMIP5 models. Comparison of permafrost distributions with respect to eight sets of reanalysis data showed that CRU_CFSR data possess the smallest AAB and thus were selected to perform the projection. The simulated ensemble mean present-day permafrost area covers an area of 15.45×10^6 km^2 decade^{-1}, which compares favorably to the area estimates of 15.24×10^6 km^2 decade^{-1} from the IPA map. Moreover, there are small differences between permafrost extents from each climate model.

The percentage trend in permafrost area indicates that the high-altitude (Tibetan Plateau) permafrost shows a faster thaw than the high-latitude permafrost. For four countries, permafrost in China has the fastest thaw speed, followed by the United States, Russia, and Canada. These discrepancies in thaw speed are mainly linked to different percentage sensitivities of permafrost areas in these different regions to air temperature change, which is further likely related to thermal conditions of permafrost in these regions.

The ensemble mean results showed that a poleward retreat occurs by the period 2080–2099 under RCP2.6, RCP4.5, and RCP6.0, and thaw mainly occurs at the southern edge of the permafrost areas. Under RCP8.5, permafrost in China, the United States, and the Tibetan Plateau will almost disappear. Permafrost in Canada will retreat to north of 65°N, and permafrost in Russia will remain mainly in the western part of the east Siberian Mountains.

The results of the present study highlight the differences of future permafrost thaw between several regions. They will be useful for understanding future permafrost degradation from the regional perspective. Further discussion showed that the present projection results are comparable with results from previous studies. Possible uncertainties in this study can primarily be attributed to the coarse horizontal resolution of climate models. Historically, research on permafrost projection has moved, in terms of methodology, from early diagnostic models driven by a fixed warming scenario [*Anisimov and Nelson*, 1996], to single general circulation model with multiple Special Report on Emissions Scenarios (SRES) scenarios [*Lawrence and Slater*, 2005; *Lawrence et al*., 2012], and then to multiple models and multiple-SRES-scenario projections [*Koven et al*., 2013; *Slater and Lawrence*, 2013]. The present study performed a multiregion comparison of future permafrost change to explore the differences between those regions using multiple models and under multiple SRES scenarios. Future work is planned that will explore regional difference of future permafrost change using dynamical climate models with a finer horizontal resolutions.

Acknowledgments
This research was jointly supported by the National Basic Research Program of China (2012CB955401) and the National Natural Science Foundation of China under grants 41130103, 41421004, and 41405087. Thanks are due to the data centers for providing various data sets for this study: the ERA-Interim reanalysis data were derived from the European Centre for Medium-Range Weather Forecasts (ECMWF); the MERRA data were derived from the Modeling and Assimilation Data and Information Services Center (MDISC), managed by the NASA Goddard Earth Sciences (GES) Data and Information Services Center (DISC); the CFSR data were obtained from the CISL Research Data Archive, managed by NCAR's Data Support Section Data for Atmospheric and Geosciences Research; the JRA-55 data were obtained from the Japan Meteorological Agency (JMA) Data Dissemination System (JDDS); the CRU data were obtained from http://www.cru.uea.ac.uk/; the CMIP5 simulation data were obtained from the Earth System Grid Federation; and the International Permafrost Association (IPA) map were obtained from the National Snow & Ice data Center (NSIDC). Thanks are also due to Professor Frederick E. Nelson, Andrew G. Slater, and David M. Lawrence for very useful help on the SFI model during preparation of this article.

References

Anisimov, O. A., and F. Nelson (1996), Permafrost distribution in the Northern Hemisphere under scenarios of climate change, *Global Planet. Change*, *14*, 59–72.

Bentsen, M., et al. (2013), The Norwegian Earth System Model, NorESM1-M-Part 1: Description and basic evaluation of the physical climate, *Geosci. Model Dev.*, *6*, 687–720.

Bi, D., et al. (2013), The ACCESS coupled model: Description, control climate and evaluation, *Aust. Met. Oceanogr. J.*, *63*, 41–64.

Brown, J., O. J. Ferrians Jr., J. A. Heginbottom, and E. S. Melnikov (1997), Circum-Arctic map of permafrost and ground-ice conditions, U.S. Geological Survey in Cooperation with the Circum-Pacific Council for Energy and Mineral Resources, Circum-Pacific Map Series CP-45, scale 1:10,000,000, 1 sheet.

Chen, H. P., J. Q. Sun, and X. L. Chen (2014), Projection and uncertainty analysis of global precipitation-related extremes using CMIP5 models, *Inter. J. Climatol.*, *34*, 2730–2748.

Cheng, G. D., and S. L. Wang (1982), On the zonation of high-altitude permafrost in China [In Chinese], *J. Glaciol. Cryopedol.*, *4*, 1–17.

Collins, M., et al. (2013), Long-term climate change: Projections, commitments and irreversibility, in *Climate Change 2013: The Physical Science Basis. Contribution of Working Group I to the Fifth Assessment Report of the Intergovernmental Panel on Climate Change*, edited by T. F. Stocker et al., Cambridge Univ. Press, Cambridge, U. K., and New York.

Dee, D. P., et al. (2011), The ERA-Interim reanalysis: Configuration and performance of the data assimilation system, *Q. J. R. Meteorol. Soc.*, *137*, 553–597.

Flato, G. M., G. J. Boer, W. G. Lee, N. A. McFarlane, D. Ramsden, M. C. Reader, and A. J. Weaver (2000), The Canadian Centre for Climate Modeling and Analysis global coupled model and its climate, *Clim. Dyn.*, *16*, 451–467.

Gent, P. R., et al. (2011), The Community Climate System Model version 4, *J. Clim.*, *24*, 4973–4991.

Guo, D. L., M. X. Yang, and H. J. Wang (2011a), Characteristics of land surface heat and water exchange under different soil freeze/thaw conditions over the central Tibetan Plateau, *Hydrol. Process.*, *25*, 2531–2541.

Guo, D. L., M. X. Yang, and H. J. Wang (2011b), Sensible and latent heat flux response to diurnal variation in soil surface temperature and moisture under different freeze/thaw soil conditions in the seasonal frozen soil region of the central Tibetan Plateau, *Environ. Earth Sci.*, *63*, 97–107.

Guo, D. L., H. J. Wang, and D. Li (2012), A projection of permafrost degradation on the Tibetan Plateau during the 21st century, *J. Geophys. Res.*, *117*, D05106, doi:10.1029/2011JD016545.

Guo, D. L., and H. J. Wang (2013), Simulation of permafrost and seasonally frozen ground conditions on the Tibetan Plateau, 1981–2010, *J. Geophys. Res. Atmos.*, *118*, 5216–5230, doi:10.1002/jgrd.50457.

Guo, D. L., and H. J. Wang (2014), Simulated change in the near-surface soil freeze/thaw cycle on the Tibetan Plateau from 1981 to 2010, *Chin. Sci. Bull.*, *59*, 2439–2448.

Guo, D. L., and J. Q. Sun (2015), Permafrost thaw and associated settlement hazard onset timing over the Qinghai-Tibet engineering corridor, *Int. J. Disaster Risk Sci.*, *6*, 347–358.

Harris, I., P. D. Jones, T. J. Osborn, and D. H. Lister (2014), Updated high-resolution grids of monthly climatic observations—the CRU TS3.10 dataset, *Int. J. Climatol.*, *34*, 623–642.

IPCC (2013), Summary for policymakers, in *Climate Change 2013: The Physical Science Basis. Contribution of Working Group I to the Fifth Assessment Report of the Intergovernmental Panel on Climate Change*, edited by T. F. Stocker et al., Cambridge Univ. Press, Cambridge, U. K., and New York.

James, W. H., et al. (2013), The Community Earth System Model: A framework for collaborative research, *Bull. Am. Meteorol. Soc.*, *94*, 1339–1360.

Jeffrey, S. J., L. D. Rotstayn, M. A. Collier, S. M. Dravitzki, C. Hamalainen, C. Moeseneder, K. K. Wong, and J. I. Syktus (2013), Australia's CMIP5 submission using the CSIRO Mk3.6 model, *Aust. Met. Oceanogr. J.*, *63*, 1–13.

Kobayashi, S., et al. (2015), The JRA-55 Reanalysis: General specifications and basic characteristics, *J. Meteorol. Soc. Jpn.*, *93*, 5–48.

Koven, C. D., W. J. Riley, and A. Stern (2013), Analysis of permafrost thermal dynamics and response to climate change in the CMIP5 Earth System Models, *J. Clim.*, *2013*(26), 1877–1900.

Lachenbruch, A., and B. Marshall (1986), Changing climate: Geothermal evidence from permafrost in the Alaskan Arctic, *Science*, *234*, 689–696.

Lawrence, D. M., and A. G. Slater (2005), A projection of severe near-surface permafrost degradation during the 21st century, *Geophys. Res. Lett.*, *32*, L24401, doi:10.1029/2005GL025080.

Lawrence, D. M., A. G. Slater, V. E. Romanovsky, and D. J. Nicolsky (2008), Sensitivity of a model projection of near-surface permafrost degradation to soil column depth and representation of soil organic matter, *J. Geophys. Res.*, *113*, F02011, doi:10.1029/2007JF000883.

Lawrence, D. M., A. G. Slater, and S. C. Swenson (2012), Simulation of present-day and future permafrost and seasonally frozen ground conditions in CCSM4, *J. Clim.*, *25*, 2207–2225.

Li, X., R. Jin, X. Pan, T. Zhang, and J. Guo (2012), Changes in the near-surface soil freeze-thaw cycle on the Qinghai-Tibetan Plateau, *Int. J. Appl. Earth Obs. Geoinform.*, *17*, 33–42.

Liu, Y., and D. B. Jiang (2016a), Mid-Holocene permafrost: Results from CMIP5 simulations, *J. Geophys. Res. Atmos.*, *121*, 221–240, doi:10.1002/2015JD023837.

Liu, Y., and D. B. Jiang (2016b), Last glacial maximum permafrost in China from CMIP5 simulations, *Palaeogeogr. Palaeoclimatol. Palaeoecol.*, *447*, 12–21.

Muller, S. W. (1947), *Permafrost or Permanently Frozen Ground and Related Engineering Problems*, 231 pp., J. W. Edwards, Ann Arbor.

Nakicenovic, N., et al. (2000), Emissions scenarios, in *A Special Report of Working Group III of the Intergovernmental Panel on Climate Change*, 599 pp., Cambridge Univ. Press, Cambridge, U. K., and New York.

Burn, C. R., and F. E. Nelson (2006), Comment on "A projection of severe near-surface permafrost degradation during the 21st century" by David M. Lawrence and Andrew G. Slater, *Geophys. Res. Lett.*, *33*, L21503, doi:10.1029/2006GL027077.

Nelson, F. E., O. A. Anisimov, and N. I. Shiklomanov (2002), Climate change and hazard zonation in the circum-Arctic permafrost regions, *Nat. Hazard.*, *26*, 203–225.

Nelson, F., and S. Outcalt (1987), A computational method for prediction and regionalization of permafrost, *Arct. Alp. Res.*, *19*, 279–288.

Rienecker, M. M., et al. (2011), MERRA: NASA's Modern-Era Retrospective Analysis for Research and Applications, *J. Clim.*, *24*, 3624–3648.

Saha, S., et al. (2010), The NCEP Climate Forecast System Reanalysis, *Bull. Am. Meteorol. Soc.*, *91*, 1015–1057.

Schmidt, G. A., et al. (2014), Configuration and assessment of the GISS ModelE2 contributions to the CMIP5 archive, *J. Adv. Model. Earth Syst.*, *6*, 141–184, doi:10.1002/2013MS000265.

Schuur, E., J. Vogel, K. Crummer, H. Lee, J. Sickman, and T. Osterkamp (2009), The effect of permafrost thaw on old carbon release and net carbon exchange from tundra, *Nature*, *459*, 556–559.

Scoccimarro, E., S. Gualdi, A. Bellucci, A. Sanna, P. G. Fogli, E. Manzini, M. Vichi, P. Oddo, and A. Navarra (2011), Effects of tropical cyclones on ocean heat transport in a high resolution coupled general circulation model, *J. Clim.*, *24*, 4368–4384.

Slater, A. G., and D. M. Lawrence (2013), Diagnosing present and future permafrost from climate models, *J. Clim.*, *26*, 5608–5623.

Stendel, M., and J. Christensen (2002), Impact of global warming on permafrost conditions in a coupled GCM, *Geophys. Res. Lett.*, *29*(13), 1632, doi:10.1029/2001GL014345.

Taylor, K. E., R. J. Stouffer, and G. A. Meehl (2012), An overview of CMIP5 and the experiment design, *Bull. Am. Meteorol. Soc.*, *93*, 485–498.

Tjiputra, J. F., C. Roelandt, M. Bentsen, D. M. Lawrence, T. Lorentzen, J. Schwinger, Ø. Seland, and C. Heinze (2013), Evaluation of the carbon cycle components in the Norwegian Earth System Model (NorESM), *Geosci. Model Dev.*, *6*, 301–325.

Voldoire, A., et al. (2013), The CNRM-CM5.1 global climate model: Description and basic evaluation, *Clim. Dyn.*, *40*, 2091–2121.

Volodin, E. M., N. A. Dianskii, and A. V. Gusev (2010), Simulating present-day climate with the INMCM4. 0 coupled model of the atmospheric and oceanic general circulations, *Izvestiya, Atmos. Oceanic Phys.*, *46*, 414–431.

Watanabe, M., et al. (2010), Improved climate simulation by MIROC5: Mean states, variability, and climate sensitivity, *J. Clim.*, *23*, 6312–6335.

Watanabe, S., et al. (2011), MIROC-ESM 2010: Model description and basic results of CMIP5-20c3m experiments, *Geosci. Model Dev.*, *4*, 845–872.

Wu, T., R. Yu, F. Zhang, Z. Wang, M. Dong, L. Wang, X. Jin, D. Chen, and L. Li (2010), The Beijing Climate Center atmospheric general circulation model: Description and its performance for the present-day climate, *Clim. Dyn.*, *34*, 123–147.

Yan, Q., H. J. Wang, O. M. Johannessen, and Z. S. Zhang (2014), Greenland ice sheet contribution to future global sea level rise based on CMIP5 models, *Adv. Atmos. Sci.*, *31*, 8–16.

Yang, M. X., F. Nelson, N. Shiklomanov, D. L. Guo, and G. Wan (2010), Permafrost degradation and its environmental effects on the Tibetan Plateau: A review of recent research, *Earth Sci. Rev.*, *103*, 31–44.

Yukimoto, S., et al. (2011), Meteorological research institute earth system model version 1 (MRI-ESM1): Model description, Technical Report of the Meteorological Research Institute, 64, 83 pp.

Yukimoto, S., et al. (2012), A new global climate model of the Meteorological Research Institute: MRI-CGCM3—Model description and basic performance, *J. Meteorol. Soc. Jpn.*, *90A*, 23–64.

Zhang, T., R. G. Barry, K. Knowles, J. A. Heginbottom, and J. Brown (1999), Statistics and characteristic of permafrost and ground-ice distribution in the Northern Hemisphere, *Polar Geogr.*, *23*, 132–154.

Zimov, S., E. Schuur, and F. Chapin III (2006), Permafrost and the global carbon budget, *Science*, *312*, 1612–1613.